JGR Solid Earth

RESEARCH ARTICLE
10.1029/2019JB018668

Radiometric Temperature Measurements in Nongray Ferropericlase With Pressure- Spin- and Temperature-Dependent Optical Properties

Sergey S. Lobanov[1] and Sergio Speziale[1]

[1]GFZ German Research Center for Geosciences, Potsdam, Germany

Abstract Accurate temperature determination is central to measurements of physical and chemical properties in laser-heated (LH) diamond anvil cells (DACs). Because the optical properties of samples at high pressure-temperature (P-T) conditions are generally unknown, virtually all LH DAC studies employ the graybody assumption (i.e., wavelength-independent emissivity and absorptivity). Here we test the adequacy of this assumption for ferropericlase (13 mol.% Fe), the second most abundant mineral in the Earth's lower mantle. We model the wavelength-dependent emission and absorption of thermal radiation in samples of variable geometry and with absorption coefficients experimentally constrained at lower mantle P and P-T. The graybody assumption in LH DAC experiments on nongray ferropericlase contributes moderate systematic errors within ±200 K at 40, 75, and 135 GPa and T < 2300 K for all plausible sample geometries. However, at core-mantle boundary P-T conditions (135 GPa, 4000 K) the graybody assumption may underestimate the peak temperature in the DAC by up to 600 K in self-insulated samples due to selective light attenuation in highly opaque ferropericlase. Our results allow insights into the apparent discrepancy between available ferropericlase melting studies and offer practical guidance for accurate measurements of its solidus in LH DACs. More generally, the results of this work demonstrate that reliable temperature measurements in LH DACs require that the optical and geometrical properties of the samples are established.

Plain Language Summary Here we modeled how colored samples affect temperature measurements in laser-heated diamond anvil cell experiments. We show that the systematic error in temperature may be large if the wavelength dependence of the sample's optical properties is not considered. The extant discrepancy in the ferropericlase melting curves at lower mantle conditions may originate from the improper assumption of its optical properties.

Key Points:
- The community-wide graybody assumption in radiometric temperature measurements may produce systematic errors in T up to 600 K
- Previous reports on ferropericlase solidus curves at lower mantle P-T may suffer from strongly nongray sample properties
- Optical properties of mantle phases at appropriate P-T are needed for accurate temperature measurements by radiometry in diamond anvil cells

Supporting Information:
- Data S1
- Table S2

Correspondence to:
S. S. Lobanov,
slobanov@gfz-potsdam.de

Citation:
Lobanov, S. S., & Speziale, S. (2019). Radiometric temperature measurements in nongray ferropericlase with pressure- spin- and temperature-dependent optical properties. *Journal of Geophysical Research: Solid Earth*, *124*, 12,825–12,836. https://doi.org/10.1029/2019JB018668

Received 6 SEP 2019
Accepted 13 DEC 2019
Accepted article online 14 DEC 2019
Published online 30 DEC 2019
Corrected 30 APR 2020

This article was corrected on 30 APR 2020. See the end of the full text for details.

©2019. The Authors.
This is an open access article under the terms of the Creative Commons Attribution License, which permits use, distribution and reproduction in any medium, provided the original work is properly cited.

1. Introduction

Temperature measurements in laser-heated (LH) diamond anvil cells (DACs) provide crucial information to determine the properties of geomaterials within deep planetary interiors. Today, direct characterization of sample density, elasticity, and phase transitions as a function of pressure-temperature (*P-T*; Andrault et al., 2011; Andrault et al., 2014; Fiquet et al., 2010; Grocholski et al., 2012; Nomura et al., 2014; Shim et al., 2001; Zerr et al., 1998) sets the base for the interpretation of global seismic velocity models as well as local seismic discontinuities within Earth's interior (Dziewonski & Anderson, 1981; Megnin & Romanowicz, 2000). Other important physical and chemical properties (e.g., transport properties) of relevant materials can also be probed in situ (Hasegawa et al., 2019; Konopkova et al., 2016; McWilliams et al., 2015; Ohta et al., 2010; Ohta et al., 2017). Accordingly, the accuracy of temperature measurements in LH DACs affects our understanding of the structure and dynamics of the deep Earth and is of primary importance to geosciences.

The community-wide yardstick for temperature measurements in LH DACs has been the fit of Planck's law to sample's thermal emission spectrum, which yields temperature as a fitting parameter (Benedetti & Loubeyre, 2004; Campbell, 2008; Kunz et al., 2018; Ming & Bassett, 1974; Prakapenka et al., 2008). Several sources of ambiguity are associated with radiometric temperature measurements in LH DAC experiments (Benedetti et al., 2007; Giampaoli et al., 2018; Walter & Koga, 2004). Notably, previous studies showed that the spectral sampling of radial and axial temperature gradients, which are unavoidable if a near-infrared

(IR; e.g., Nd:YAG or Nd:YLF) heating laser is employed but can be mitigated by using a mid-IR CO_2 laser (Petitgirard et al., 2014), lead to the underestimation of the sample's maximum temperature by up to 10 % (Kavner & Panero, 2004; Manga & Jeanloz, 1996). While temperature gradients have being well recognized as a systematic source of error, the reported temperatures (e.g., melting temperatures) are rarely corrected for such gradients and a cumulative uncertainty of ±150 K is usually presumed. Yet there is another systematic and potentially important source of error that is virtually never considered. The determination of temperature by Planck fitting in LH DAC experiments relies on the assumption of wavelength-independent emissivity (graybody approximation), which comes as a second free parameter into the fitting. Wavelength-dependent emissivity of mantle minerals has never been characterized at appropriate *P*-*T* conditions due to associated experimental challenges, hence the ubiquity of the graybody assumption. Iron-bearing mantle minerals, however, are nongray semitransparent solids and may show strongly wavelength-dependent optical properties (e.g., emissivity) at 600–900 nm (Dubrovinsky et al., 2008; Goncharov et al., 2006; Goncharov et al., 2015; Keppler et al., 1994; Keppler et al., 2007; Keppler & Smyth, 2005; Lobanov et al., 2017; Lobanov et al., 2017; Thomas et al., 2012; Ullrich et al., 2002), which is a common spectral range used for radiometric measurements in LH DACs. The application of Kirchhoff's law of radiation to a partially transparent body entails that the emissive and absorptive powers of the body at a given wavelength are equal if light reflections are negligible (McMahon, 1950), a condition that is to first order satisfied in LH DACs on mantle minerals (Goncharov et al., 2009). Accordingly, the graybody approximation can be lifted if the absorption coefficient is known.

Several physical mechanisms may contribute to light absorption at 600–900 nm in iron-bearing phases: (i) multiplicity-allowed *d*-*d* electron transfer (crystal field transitions), (ii) intervalence (e.g., Fe^{2+}- Fe^{3+}) charge transfer (CT), and (iii) Fe-O CT (Burns, 1993). Position and intensity of associated absorption bands are *P*-, *T*-, iron concentration-, and material-dependent; thus, the absorption coefficients of major mantle minerals have to be mapped onto their stability fields in order to move beyond the graybody approximation. This is a formidable task as the conventional light sources used for optical absorption measurements are not bright enough to probe hot radiating samples. Because of this experimental challenge, high-pressure high-temperature absorption spectra of Earth's two most abundant minerals, bridgmanite (Bgm) and ferropericlase (Fp), are not yet available.

Of these two phases Fp is particularly important as its iron content in the lower mantle is higher than in Bgm (e.g., Piet et al., 2016) and, consequently, Fp has a stronger light absorption coefficient, which may affect the analysis of thermal radiance for temperature determination in LH DACs. In addition, iron in Fp undergoes a spin transition at 50–70 GPa (at 300 K; Badro, 2014; Badro et al., 2003; Glazyrin et al., 2016; Lin et al., 2006; Lin et al., 2013; Speziale et al., 2005), which modifies the number and intensity of absorption bands in the visible and near-IR range (Goncharov et al., 2006; Keppler et al., 2007). Accordingly, thermal radiance of Fp across the temperature-induced high-to-low spin transition integrates the effect of a continuous change in Fp optical properties, which have never been considered in determining temperature in LH DAC experiments at $P > 50$ GPa, such as, for example, in studies of Fp spin state diagram (Lin et al., 2007).

Deng et al. (2017) have explored the effect of wavelength-dependent absorption coefficient on the temperature determination by radiometry under the graybody assumption. Comparing their results to measured room-temperature high-pressure Fp absorption coefficients, the authors concluded that wavelength-dependent emissivity and absorptivity contribute a systematic error of up to 700 K to the measurements of the melting onset in Fp (Deng et al., 2017). To correct for nongray sample behavior, however, one not only needs to know the optical properties of the sample but also the sample thickness and the temperature profile across it. Combining ex post analysis of sample geometry with appropriate models of heat fluxes in a LH DAC and available estimates of Fp optical properties, Deng and Lee (2017) corrected for the nongray behavior and reported solidus and liquidus temperatures of Fp solid solutions. Their solidus/liquidus curves show a sharp depression at ~50 GPa, correlating with the spin transition pressure (Deng & Lee, 2017, 2019), and are ~500 K below the solidus/liquidus curves reported by Fu et al. (2018), who did not correct the measured temperatures for nongray Fp. On its face, the melting curves of Deng and Lee (2017) should be preferred because the temperature correction is justified for Fp. However, their temperature correction relies heavily on the absorption coefficients of Fp at high pressure, which are available only for selected compositions and exclusively at room temperature. Here we attempt to reconcile the discrepant Fp melting data by considering several independent cases with *P*-, spin-, and *P*-*T*-dependent optical properties of Fp with 13 mol.% Fe that

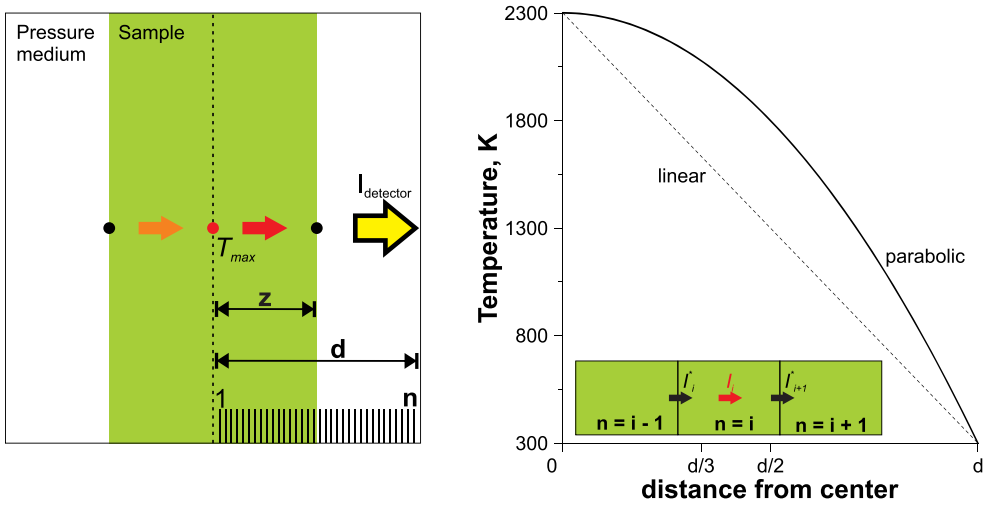

Figure 1. 1-D radiation transport model. (left) Geometry and input parameters: sample's half-thickness (z), diamond anvil cell cavity half-thickness (d), and number of slabs with distinct temperature ($n = 10^3$); T_{max} is the temperature at the center of the sample. The model quantifies $T_{apparent}$ by fitting the Planck's law to the thermal radiation spectrum that reaches the detector ($I_{detector}$). (right) Examples of two input temperature profiles (linear and parabolic) with $T_{max} = 2300$ K. (inset) The thermal emission of the ith slab (I_i) is added to the light that enters the ith slab from the (i−1) slab (I^*_i). These two contributions are attenuated by the absorbance of the ith slab and passed to the (i+1) slab (I^*_{i+1}).

we measured at appropriate *P-T* (and spin state) conditions. Our results have implications for the presence/absence of (Mg,Fe)O melt in the lowermost mantle and its chemical composition, which are among the key unknowns in elucidating the nature of seismically observed ultralow-velocity zones (Bower et al., 2011; Wicks et al., 2017; Williams & Garnero, 1996; Yuan & Romanowicz, 2017), and are thus of primary importance to geosciences.

2. Materials and Methods

2.1. 1-D Radiation Transport Model

Flat, single-crystalline ferropericlase (thickness 2z) is placed in the center of the DAC gasket cavity (thickness 2d) and surrounded by nonabsorbing pressure medium that also provides thermal insulation (Figure 1). Double-sided near-IR laser heating produces steep symmetric temperature profiles across the sample due to the very high thermal conductivity of the diamond anvils, which remain essentially at 300 K (Bodea & Jeanloz, 1989; Kiefer & Duffy, 2005; Petitgirard et al., 2014; Rainey et al., 2013). The shape of the temperature profile is most sensitive to the absorption coefficient at the heating wavelength, the presence of thermal insulator/pressure medium, its thickness, and the sample to insulation thermal conductivity ratio (Kiefer & Duffy, 2005; Montoya & Goncharov, 2012). Several characteristic temperature profiles have been revealed in finite-element models of thermal fluxes in LH DACs as a function of these parameters. Insulators and metals, in particular, develop notably different temperature profiles due to different penetration depths of the heating laser (Gomez-Perez et al., 2017; Konopkova et al., 2016; Manga & Jeanloz, 1996; Montoya & Goncharov, 2012; Panero & Jeanloz, 2001; Rainey et al., 2013). Usually, insulators have the maximum temperature at the center of the partially absorbing sample while metals at its interfaces with the pressure medium. In this study we treat ferropericlase as an insulator in the entire range of *P-T* conditions (Ohta et al., 2017) and, for simplicity, assume a linear (L) and a parabolic (P) temperature profile in a sample with a constant thermal conductivity (Manga & Jeanloz, 1996; Figure 1, right). We chose the L and P profiles to qualitatively assess the effect of variable axial T gradients rather than as good approximations of the steady-state temperature distributions in dielectric samples loaded in a LH DACs. One additional oversimplification in our approach is that we do not adjust the axial T profile for a changing sample filling fraction and thickness. We expect that more realistic temperature profiles produced by double-sided laser heating of Fp surrounded by a pressure medium (KCl, NaCl, MgO, or Al_2O_3) as well as in self-insulating Fp samples fall in between the L and P cases (e.g.Kiefer & Duffy, 2005, Manga & Jeanloz, 1996, Montoya & Goncharov, 2012)

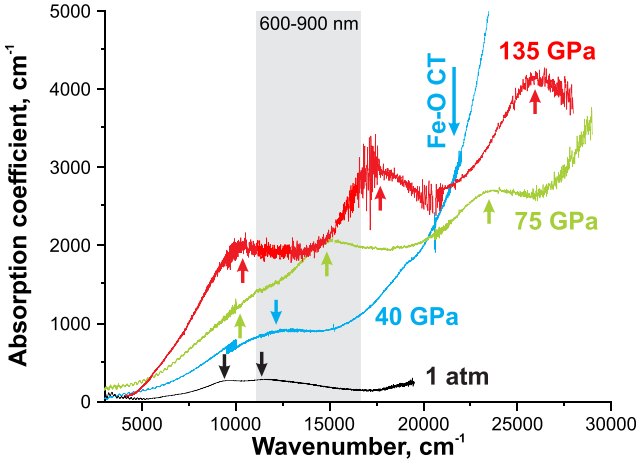

Figure 2. Room-temperature absorption coefficients of ferropericlase Fp_{13} (13 mol.% Fe) at 1 atm (black), 40 (blue), 75 (green), and 135 (red) GPa. The gray area depicts the spectral range typical of temperature measurements by radiometry in laser-heated diamond anvil cell experiments. Crystal field (*d*-*d*) band(s) and Fe-O charge transfer are marked with arrows.

due to their thermal properties at high *P*-*T* (Andersson, 1985; Ohta et al., 2017). Therefore, the use of these simplified cases is justified for the purposes of this study.

Half of the DAC cavity is sliced evenly into n slabs each of which is assigned its temperature based on the input axial temperature profile ranging from T_{max} in the center to 300 K at the diamond tip (Figure 1). The thermal spectrum emitted from an ith slab is given by Planck's law of blackbody radiation scaled by the slab's emissivity:

$$I_i(\lambda) = \epsilon_i(\lambda)\frac{2hc^2}{\lambda^5}\frac{1}{e^{\frac{hc}{\lambda k T_i}}-1} \quad (1)$$

where c, h, and k are the speed of light, Planck, and Boltzmann constants, respectively; λ is wavelength; $\epsilon_i(\lambda)$ is wavelength-dependent emissivity; and T_i is the temperature of the ith slab. The emissivity is given by the Kirchhoff's law for partially transparent bodies (McMahon, 1950):

$$\epsilon_i(\lambda) = 1-10^{-\alpha_i(\lambda)\times\left(\frac{d}{n}\right)/\ln 10} \quad (2)$$

where $\alpha_i(\lambda)$ is the wavelength-dependent absorption coefficient of the ith slab. Typical pressure media/thermal insulators used in LH DAC experiments (MgO, NaCl, KCl, and Al_2O_3) are wide bandgap insulators and do not absorb light at 600–900 nm, and we assume that the emissivity of the pressure medium is zero.

Individual slabs emit, attenuate, and transmit thermal radiation:

$$I^*_{i+1}(\lambda) = \left(I^*_i(\lambda) + I_i(\lambda)\right)\times 10^{A_i(\lambda)} \quad (3)$$

where $I^*_{i+1}(\lambda)$ is the thermal emission spectrum that is passed to the next slab after light emission and attenuation in the ith slab (Figure 1, inset); $A_i(\lambda)$ is ith slab's absorbance. Although only half the sample is modeled, we compute the spectral contributions from the entire sample (as schematically shown by orange and red arrows in Figure 1). The sum of these contributions is the total light that reaches the detector ($I_{detector}$). By fitting Planck's law to $I_{detector}$ in the 600- to 900-nm spectral range we obtain $T_{apparent}$ and a single value for emissivity (wavelength-independent). This procedure simulates a common LH DAC experiment with radiometric temperature measurements under the graybody assumption. For computational efficiency we set n to 10^3 as the output results of these models are within 1 K to that of models run with $n = 10^4$. Radial temperature gradients are not considered in this work but would lower the apparent temperatures because of the spectral sampling of colder regions (Kavner & Panero, 2004; Panero & Jeanloz, 2001).

2.2. Input Parameters

To constrain the input parameters for the 1-D Radiation Transport Model, we measured the absorption coefficient of a Fp sample (Fp_{13}: 13 mol.% Fe; Fe^{3+}/Fe_{total} ~10 %) at 1 atm (3,000–19,500-cm^{-1} spectral range) and at 40, 75, and 135 GPa (3,000–30,000 cm^{-1}; Figure 2). Optical-quality single-crystalline Fp was synthesized by diffusing Fe into an MgO single crystal sandwiched between platelets of $(Mg_{0.8},Fe_{0.2})O$ powder at 1 atm in a gas-mixing furnace. After the synthesis, the single crystal of Fp was double-polished down to ~16 μm with a 3- and 1-μm diamond grit, followed by a 0.3-μm Al_2O_3 powder. Rectangular chips of the polished sample were washed in alcohol and loaded into the DAC sample chamber (20- to 40-μm-thick Re gasket) between dry KCl wafers (5–15 μm thick), which served as both a pressure-transmitting medium and the optical reference in absorbance measurements. Immediately after the loading, the DAC was sealed and brought to the desired pressure using ruby fluorescence (Syassen, 2008) and/or the diamond Raman edge (Akahama & Kawamura, 2006) as a pressure gauge. The discrepancy between the two pressure readings was within 5%. Details on the experimental setup used here to measure the absorption coefficients at high pressure and 300 K have been reported previously (Goncharov et al., 2009; Goncharov et al., 2015).

Optical absorbance was measured on decompression, allowing the sample thickness to change elastically (Ohta et al., 2012; Ohta et al., 2017; Okuda et al., 2017), which is important for reliable thickness estimates at high pressure. First, the thickness of decompressed samples at 1 atm was measured using a Zygo NewView 5032 optical 3-D profilometer after dissolving the KCl wafers in distilled H_2O on a clean glass slide. Next, the obtained thickness at 1 atm was adjusted upward using the MgO equation of state (Tange et al., 2009) in order to reconstruct the sample thickness at the pressure of the absorbance measurement. The obtained sample thickness at high pressure was consistent with the in situ measurement of the gasket thickness at high pressure by visible light interferometry after scaling by the refractive index of KCl extrapolated to 135 GPa exploiting its linear increase with density (Johannsen et al., 1997), which we calculated by using the KCl equation of state by Dewaele et al. (2012). Finally, the high-pressure absorption coefficients were obtained by scaling the sample absorbance by its thickness (and ln(10), see equation (2)). Based on the agreement between the thicknesses obtained by profilometry ex situ and that by visible light interferometry in situ, we estimate the possible error in the sample thickness to be within 20 %, which translates to the same order of ambiguity in the absorption coefficients.

At 1 atm, two distinct absorption bands are resolved in the spectrum (centered at ~9,500 and ~12,000 cm^{-1}). Both absorption components are related to a single multiplicity-allowed electronic transition: $^5T_{2g} \rightarrow {}^5E_g$, which is split by a Jahn-Teller distortion. The distortion is essentially quenched upon compression to 40 GPa where only the 12,000-cm^{-1} band is resolved. In addition, strong Fe-O CT band (seen as an absorption edge) is apparent at >15,000 cm^{-1}, a characteristic feature of many Fe-bearing minerals (Burns, 1993; Lobanov et al., 2015; Shankland et al., 1979; Ullrich et al., 2002). Across the spin transition, the single *d-d* band is replaced by three *d-d* bands, which is a consequence of the change in the multiplicity of the ground state electronic configuration. The contribution of the absorption edge to the absorption coefficient at high frequency decreases across the spin transition. Overall, these spectroscopic transformations are consistent with the previous reports on Fp optical properties at high pressure (Goncharov et al., 2006; Keppler et al., 2007). Serendipitously, the shape of the spectra at 40 and 135 GPa at 600–900 nm is qualitatively similar, while the spectrum at 75 GPa shows a relatively narrow *d-d* band almost in the center of the spectral window used for radiometric temperature measurements.

From the measured absorption coefficients, the wavelength-averaged (600–900 nm) photon mean free path ($1/\alpha$) in Fp_{13} is ~45 (1 atm), 10.9 (40 GPa), 5.7 (75 GPa), and 4.9 μm (135 GPa). These are in the range of gasket thicknesses expected for these pressures (Li et al., 2018); thus, apparent temperatures should appear sensitive not only to the Fp_{13} absorption coefficient but also to the gasket thickness ($2d$) and the DAC cavity filling ratio (z/d). To model light diffusion in nongray Fp, we set d to 10, 5, and 2.5 μm for the DAC assemblages at 40, 75, and 135 GPa, respectively. This choice is based on our own direct measurements of cavity thickness in the experiments to determine Fp_{13} absorption coefficients (by light interferometry as described above). Cavity thickness is largely governed by the mechanical properties of the gasket and pressure medium. We used Re gaskets in our spectroscopic experiments, but the obtained thicknesses are in good agreement with that reported for W gaskets at similar pressures (Li et al., 2018). The thickness of the cavity, however, would definitely be smaller in DAC experiments with stainless steel gaskets, which should be accounted for in modeling the emission/attenuation of thermal radiation in the future.

3. Results and Discussion

3.1. Temperature-Independent Absorption Coefficient at 1 atm

For an empirical demonstration of the effect of wavelength-dependent light absorption on radiometric temperature measurements, we passed the thermal emission of a W spectral calibration lamp (2 V Halogen lamp, Conrad Electronics) set to 1763 K (T_{lamp}) through a spatial filter equipped with a confocal 100-μm pinhole. The pinhole was either clear (Figure 3, case A) or covered by a 16-μm-thick Fp_{13} single-crystal platelet (case B). By fitting the Planck's law to the transmitted portion of the radiation under the graybody assumption in cases A and B we quantitatively examine the potential of nongray Fp with a thickness typical of DAC experiments to introduce systematic errors in the temperature determination. Systematically higher apparent temperatures ($T_{lamp + Fp} = T_{lamp} + 109$ K) are recorded when the pinhole is covered by Fp_{13}, in quantitative agreement with the modeled value ($T_{lamp + Fp} = T_{lamp} + 113$ K) based on the Fp_{13} absorption coefficient at 1 atm (see Figure 2, black curve), its thickness (16 μm), and the W lamp radiation

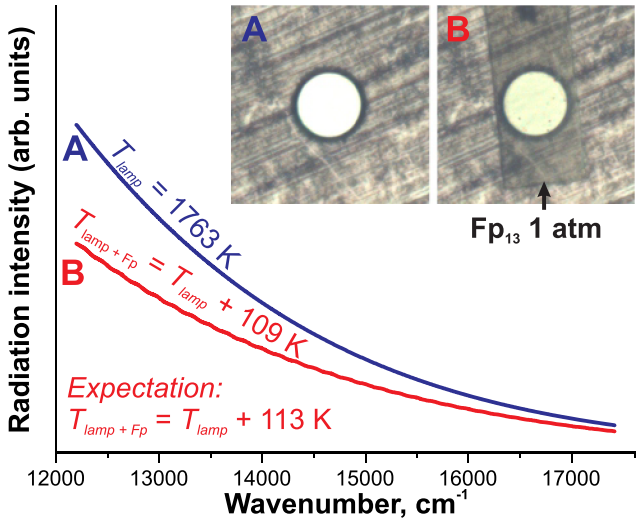

Figure 3. Measured thermal radiation spectra of a W lamp set to 1763 K through a clear 100-μm pinhole (A) and through a pinhole covered by a 16-μm-thick single crystal of Fp_{13}. Light attenuation by ferropericlase at 1 atm produces a nominally hotter spectrum (red) compared to the one emitted by the lamp (dark blue) because of the stronger absorption coefficient at near-infrared than in the visible range (Figure 2; black curve). Inset: Microphotographs of the 100-μm pinhole (A) without and (B) covered with ferropericlase platelet.

temperature of 1763 K. Higher apparent temperatures in case B are due to perturbed relative intensities in the collected spectrum after the wavelength-dependent light attenuation by Fp_{13}. At 1 atm, Fp_{13} absorbs near-IR light more efficiently than visible due to the crystal field band at ~12,000 cm^{-1}. As a result, the spectrum recorded in case B is bluer (i.e., apparently hotter) than in case A, albeit less intense. This simple experiment warrants modeling the effect of nongray Fp on temperature measurements at high pressure where the absorption coefficients are notably different from that at 1 atm.

3.2. Temperature-Independent Absorption Coefficient at High P

Here we discuss the results of the models run assuming a temperature-independent absorption coefficient of Fp_{13} at 40, 75, and 135 GPa. These models are displayed in Figure 4, where $T_{max} - T_{apparent}$ is plotted as a function of T_{max}. Models run with the Fp_{13} absorption coefficients at 40 and 135 GPa yield $T_{apparent}$ that are up to ~200 K lower (at $T_{max} = 2300$ K, linear temperature profile, $d = z$) than T_{max} as is shown in Figure 4 (left) and (right). Fp_{13} at these pressures is more absorbing in the visible than in the near-IR. The hotter the sample, the stronger the spectral overlap of its thermal emission with its absorption coefficient. As a result, shorter wavelengths are attenuated in the measured spectrum ($I_{detector}$) compared to the ideal blackbody spectrum at T_{max}, producing colder apparent temperatures. Such an effect is less pronounced in the case of the parabolic temperature profile as the sample is hotter on average.

Interestingly, the models run with small filling fractions (e.g., $d = 3z$) occasionally show nonmonotonous behavior, which may result in the change of sign of $T_{max} - T_{apparent}$. We attribute this to the competition between sample's emittance and absorbance. Samples with stronger absorption at shorter wavelengths emit bluer spectrum than a blackbody, which results in $T_{max} - T_{apparent} < 0$ if the sample is not sufficiently thick ($z < 1/\alpha$) to absorb the extra blue light in the system. Such behavior is most pronounced in the case of the parabolic temperature profile at 75 GPa with $T_{apparent}$ ~200 K higher than T_{max} at $T_{max} = 2300$ K due to the presence of the *d-d* absorption band in the middle of the 600- to 900-nm range. Here it is convenient to evaluate the physical performance of our models against that of Deng et al. (2017), who modeled the effect of the input optical thickness ($\tau = \alpha \times d$) on apparent temperature. While sample thickness was fixed in their models, the magnitude of the absorption coefficient was allowed to vary, which is similar to varying the sample thickness in our study. In a sample with

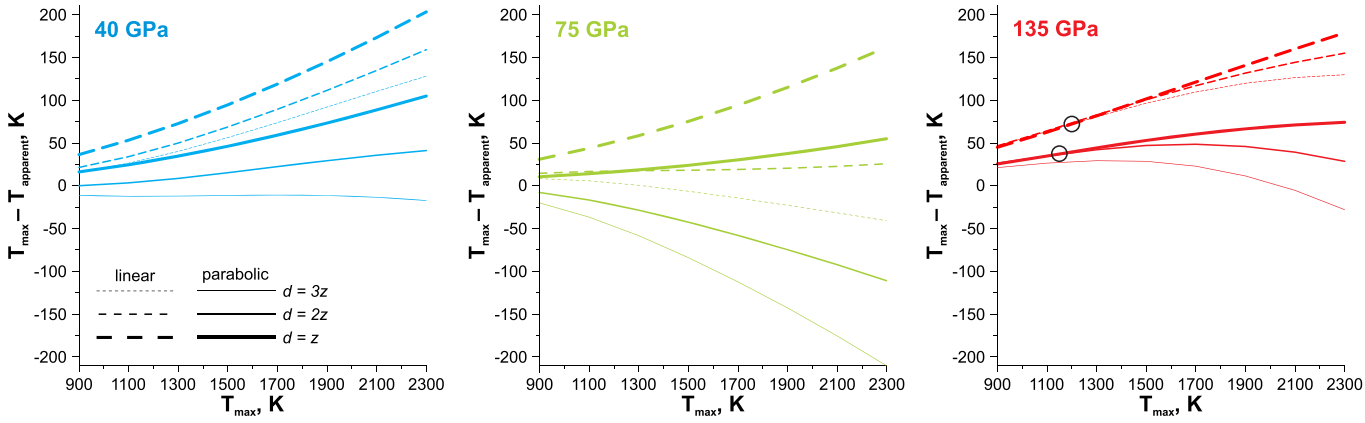

Figure 4. The effect of wavelength-dependent (but temperature-independent) light absorption in ferropericlase Fp_{13} at 40, 75, and 135 GPa on the apparent temperature. The difference ($T_{max} - T_{apparent}$) between the actual maximum temperature at the center of the sample and the temperature determined under the graybody approximation (i.e., wavelength-independent emissivity) is plotted as a function of T_{max}. Circles depict crossings of the $d = z$ and $d = 2z$ models.

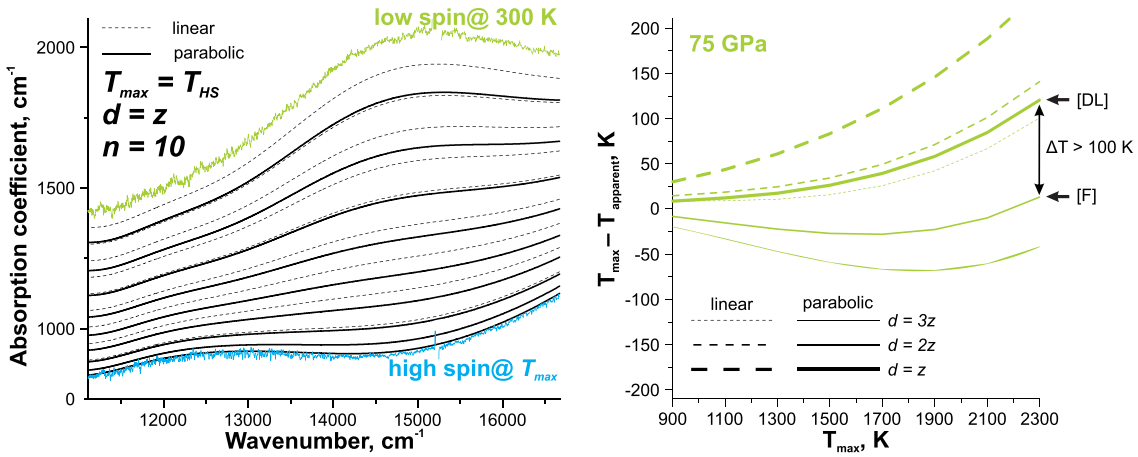

Figure 5. (left) Modeled linear combinations of the optical absorption spectra of Fp_{13} recorded at 40 (pure high spin) and 75 GPa (pure low spin). Note that the spacing between dashed lines is even for the linear temperature profile, while the solid lines are spaced closer near the high spin spectrum for the parabolic temperature profile. (right) The effect of temperature-induced low-to-high spin transition in ferropericlase at 75 GPa on the apparent temperature plotted as a function of peak temperature T_{max}. [F] and [DL] are models with geometrical parameters resembling that in the laser-heated diamond anvil cell melting experiments by Fu et al. (2018) and Deng and Lee (2017).

optical thickness that decreases with the wavelength the apparent temperatures may be both lower [large τ] and higher [small τ] than T_{max} (see Figure 5d in Deng et al., 2017). Such physical behavior is qualitatively similar to that observed in our models with temperature-invariant absorption coefficients.

Another interesting observation is that at 135 GPa the models $d = z$ and $d = 2z$ intersect at T_{max} ~ 1150–1200 K (showed by circles in Figure 4). At T_{max} < ~1200 K, there is almost no blue light in the emission spectrum and the apparent temperature is mostly governed by the lowest frequency *d*-*d* band of Fp_{13} at 135 GPa (at ~10,000 cm^{-1}) and not by the Fe-O CT band at high frequency. Therefore, the crossing of the models is due to the higher near-IR sample absorbance of the thicker ferropericlase ($d = z$ case), which is more efficient in reducing $T_{max} - T_{apparent}$ at T_{max} < ~1200 K. Although not intuitive, such peculiar behavior is qualitatively similar to that observed and modeled for the 1-atm case discussed above.

3.3. Spin-Dependent Absorption Coefficient

Available spectroscopic studies of iron-bearing minerals indicate that the width and intensity of the absorption bands are moderately sensitive to temperature (Burns, 1993; Lobanov et al., 2016; Lobanov, Holtgrewe, et al., 2017; Shankland et al., 1979; Ullrich et al., 2002). Heating typically results in band broadening, due to the participation of vibrationally excited states in the electronic transition, and a red-shift due to the thermal expansion. However, the net effect on the absorption spectrum may remain minor in the limit of T < 2000 K (e.g., (Lobanov et al., 2016; Lobanov, Holtgrewe, et al., 2017). Temperature-induced low-to-high spin transition, on the other hand, significantly changes the absorption spectrum due to the switch in the ground state electronic configuration.

We examined the potential effect of a temperature-induced spin transition by supposing a complete transformation to the high spin configuration upon heating from 300 to 2300 K at 75 GPa, as is expected from the spin state diagram of Fp (Holmstrom & Stixrude, 2015). The mixed spin absorption coefficient was modeled assuming linear combinations of the low spin ($\alpha_{75\ GPa}$) and high spin ($\alpha_{40\ GPa}$) spectra:

$$\alpha_{\text{mixed spin}} = \alpha_{75\ GPa} \times (1 - f_{HS}) + \alpha_{40\ GPa} \times f_{HS} \quad (4)$$

where f_{HS} is the high spin state fraction $f_{HS} = (T - 300)/(T_{HS} - 300)$ and T_{HS} is the temperature needed for a complete transformation to high spin Fp at 75 GPa. We set T_{HS} to 2300 K to reflect the expected temperature-induced low-to-high spin transition of Fp at 75 GPa (Holmstrom & Stixrude, 2015). We note that the increase in the high spin fraction with temperature may be nonlinear (especially in approaching pure low and high spin states; Lin et al., 2007; Sturhahn et al., 2005; Tsuchiya et al., 2006) and our assumption of a linear relation between the spin fraction and temperature allows only qualitative conclusions. The use of the 40 GPa

room-temperature spectrum (high spin) as a first-order approximation of the Fp_{13} spectrum at 75 GPa and 2300 K (high spin) is appropriate because at these conditions Fp_{13} has the same ground state configuration ($^5T_{2g}$). Also, the energy of the $^5T_{2g} \rightarrow {}^5E_g$ transition at 75 GPa and 2300 K is similar to that at 40 GPa and 300 K because the crystal field splitting energy reduces with temperature (opposite to the pressure effect at constant temperature; Burns, 1993). One important benefit of our linear mixing approach is that it allows assigning an individual absorption coefficient to each modeled slab of Fp_{13} based on its temperature. The linear temperature profile across the sample produces slabs with evenly spaced absorption coefficients, while the parabolic profile yields slabs with absorption coefficients grouping near the spectrum characteristic of T_{max}. The produced mixed spin absorption spectra (Figure 5, left) resemble that directly measured in siderite ($FeCO_3$) upon its temperature-induced low-to-high spin transition at $T <$ ~1500 K and $P =$ 45–55 GPa (Lobanov et al., 2016), which is a consequence of the similarity of Fp and siderite iron valence and spin configurations at 40–75 GPa.

The model results for the case of spin-dependent optical properties can be viewed as a combination of the temperature-independent cases at 40 and 75 GPa (Figure 5, right). When $T_{max} <$ 1500 K (that is below T_{HS}), the model results resemble that of the 75 GPa case shown in the previous section (temperature-independent absorption spectrum). At $T_{max} >$ 1500 K significant part of the sample is in the high spin configuration, and the results for the spin-dependent model are similar to that of the spin-independent model at 40 GPa. Overall, the spin-dependent case allows assessing the magnitude of the systematic error in temperature determination introduced by the graybody approximation in high *P-T* experiments on Fp across its spin transition. Our models suggest that such an error in LH DAC experiments with in situ probing of the Fp spin state would be small: -75 K $< T_{max} - T_{apparent} < 0$ K (thermally insulated Fp and parabolic T profile). This result, however, is not necessarily characteristic of the systematic error in temperature determination in the spin transition study by Lin et al. (2007) as their sample was richer in Fe (25 mol.% Fe) and thus more absorbing than Fp_{13} modeled here.

Noninsulated samples may result in larger systematic errors ($T_{max} - T_{apparent} >$ 100 K at $T_{max} =$ 2300 K). Therefore, another application of our results is to the potential discrepancy between temperature determinations in Fp in the presence of a thick layer of pressure medium and without it. Our models with parabolic temperature gradient and a filling fraction of $d = 2z$ [F] (Figure 5, right) are representative of the melting experiments by Fu et al. (2018), based on the reported experimental details. For these input parameters our models yield a systematic error of <30 K at all temperatures below 2300 K, which is negligible in the view of the overall uncertainties in temperature, pressure in LH DAC experiments. Our model with $d = z$ [DL] and parabolic temperature profile is more adequate to describe the experiments by Deng and Lee (2017) and shows that at $T_{max} =$ 2300 K the apparent temperature is ~120 K lower. The difference between the apparent temperatures $T_{apparent}$[F] $- T_{apparent}$[DL] increases with T_{max}. This result suggests that the presence/absence of the pressure medium may be the source of the discrepancy in the reported Fp solidus temperatures at $P >$ 50 GPa in the studies by Fu et al. (2018; $T_{solidus}$ ~ 4000 K at 50 GPa) and Deng and Lee (2017; $T_{solidus}$ ~ 3500 K at 50 GPa). Even though Deng and Lee corrected for nongray Fp by assuming temperature-independent absorption spectra of low spin Fp, such correction may not be adequate at these pressures because of the unavoidable temperature-induced low-to-high spin transition in Fp (Holmstrom & Stixrude, 2015; Lin et al., 2007). We note, however, that this inference may not be conclusive because (i) the melting temperature of Fp is above 3500 K at $P >$ 75 GPa and Fp absorption coefficients at comparable temperatures are needed to properly address the discrepancy in the published Fp melting curves and (ii) our models may be inadequate for modeling experiments with nonnegligible melt fractions whose optical properties are unknown.

3.4. Temperature-Dependent Absorption Coefficient

Our recent measurements of Fp opacity in the visible and near-IR range by a streak camera (performed on the same sample as studied here) recorded a rapid temperature-induced red-shift of the Fe-O CT band at 135 GPa up to 4000 K (Lobanov et al., 2019). The resulting absorption coefficient of Fp_{13} at T ~ 4000 K is very high ($\alpha =$ 6,000–9,000 cm^{-1} in the range of 600–900 nm), featureless (no distinct absorption bands), and has a characteristic negative slope ($\alpha_{600\ nm}/\alpha_{900\ nm}$ ~1.5–2). The observed rates of increase in mean Fp opacity (α/T) at 600–900 nm are ~1–2 cm^{-1}/K (averaged over the 300–4000 K range). Here we model the effect of these profound temperature-induced changes in Fp absorbance by assuming a linear absorption spectrum at

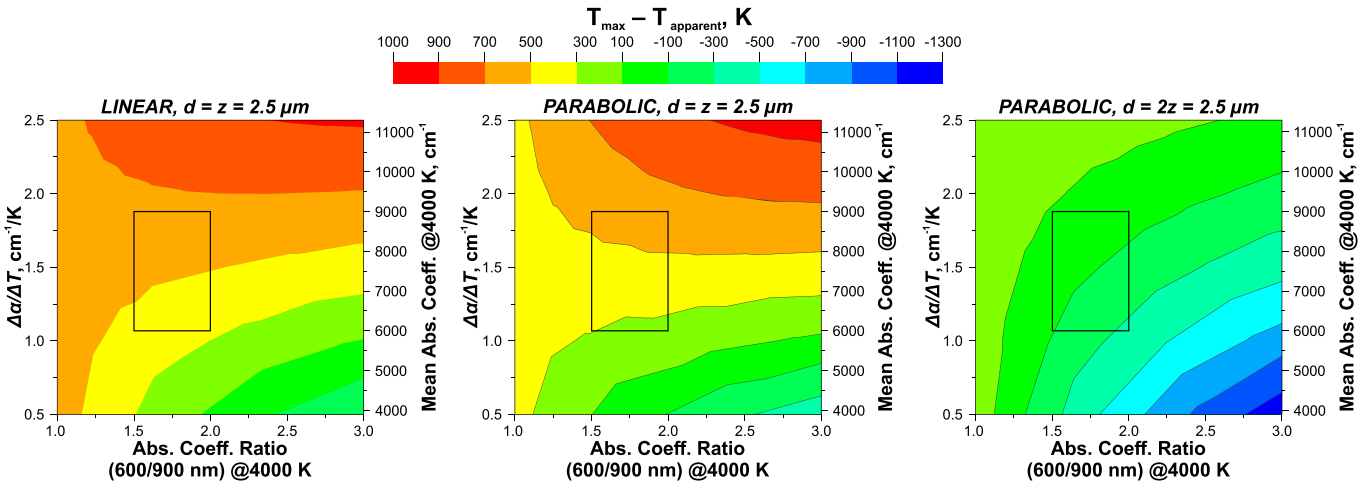

Figure 6. The effect of temperature-dependent absorption coefficient on the apparent temperature at 135 GPa and T_{max} = 4000 K as a function of the input model parameters and the mean absorption coefficient (600–900 nm) at P = 135 GPa, T_{max} = 4000 K). (left) Linear temperature profile, $d = z$ = 2.5 μm; (center) parabolic temperature profile, $d = z$ = 2.5 μm; (right) parabolic temperature profile, $d = 2z$ = 2.5 μm. The black box depicts experimentally constrained optical properties of Fp_{13} at ~135 GPa and ~4000 K (Lobanov et al., 2019).

T_{max} (fixed to 4000 K) and varying its slope ($\alpha_{600\ nm}/\alpha_{900\ nm}$ between 1 and 3), and its mean absorption coefficient in the range of 4,000–11,000 cm^{-1}. We intentionally investigate a wider variation in these parameters than that experimentally observed in Fp_{13} at 135 GPa and 4000 K in order to generalize our results to systems with different optical properties, such as Fp at different P-T conditions or of a different composition, once they are established. Each of the hypothetical absorption spectra at T_{max} (as defined by the $\alpha_{600\ nm}/\alpha_{900\ nm}$ and the mean absorption coefficient at 4000 K) is combined linearly with the measured 300 K spectrum (135 GPa) to produce intermediate absorption coefficients for T = 300–4000 K that are assigned to the modeled sample slabs based on their temperature. As in the spin-dependent case discussed above, the introduction of intermediate spectra is necessary to account for the temperature-dependent absorption coefficient across the Fp in LH DAC. The resulting mixed absorption coefficients are broadly consistent with those measured in Fp_{13} at 2500 < T < 4000 K (Lobanov et al., 2019).

The results for three specific cases (Figure 6) show that the sign and magnitude of $T_{max} - T_{apparent}$ are sensitive to the rate of increase in Fp opacity with T and, to a lesser extent, to the slope of the absorption coefficient ($\alpha_{600\ nm}/\alpha_{900\ nm}$) at 4000 K. Note that these results cannot be directly compared with the models of Deng et al. (2017) as we account for the temperature-dependence of Fp absorption spectrum. Because of this important difference, our models yield apparent temperatures that are up to 700 K lower than T_{max} even if the slab at T_{max} has a spectrum with $\alpha_{600\ nm}/\alpha_{900\ nm} = 1$ (graybody behavior) owing to different $\alpha_{600\ nm}/\alpha_{900\ nm} \neq 1$ (nongray body behavior) of all the colder slabs. Regardless of the above mentioned principal distinction in the modeling, our model results tend to converge with that of Deng et al. (2017) at Fp mean absorption coefficients (at 4000 K) smaller than ~5,000 cm^{-1}.

Projecting the range of experimentally constrained absorption coefficient of Fp_{13} (135 GPa/3,000–4,000 K) onto the model results presents an important observation: the use of self-insulating samples leads to apparent temperatures that are 300–600 K lower than T_{max}, while $T_{max} - T_{apparent}$ is in the range of −300 to 100 K for the filling fraction of $d = 2z$ (Figure 6). In other words, reducing the thickness of absorbing Fp by adding a layer of thermal insulation mitigates the effect of strong absorption in a thick and relatively cold (i.e., non-insulated) sample on temperature determination. Thus, radiometric temperature measurements in Fp in this pressure-temperature range may not require a correction for nongray sample behavior, provided that the sample filling fraction is small and the optical absorption of the first melt is not significantly different from that of the coexisting solid. Future studies of Fp properties at lower mantle conditions can readily take advantage of this practical inference.

Our results offer a possible explanation for the apparent discrepancy in the Fp solidus curves of Fu et al. (2018) and Deng and Lee (2017). The very low melting curves (even after correction) reported by Deng

and Lee (2017) in experiments with self-insulating samples may be due to the combination of self-insulating sample geometry (which produces very low apparent temperatures) and the assumption of temperature-independent Fp optical properties to correct for nongray sample behavior. This assumption turns out to be inadequate for Fp at high temperature because of its strongly temperature-dependent absorption coefficients, which, however, had not yet been measured at the time of the study by Deng and Lee (2017). As a result, the temperature correction applied by the authors was rather small (+ ~50–100 K at 80 GPa) due to the underestimated Fp opacity at high temperature. We suppose that if the optical properties of Fp at high *P-T* were available to the authors, their temperature correction may have yielded melting curves above the ones they reported and likely in a better agreement with the results of Fu et al. (2018). The experimental sample geometry used in our work, however, is not adequate for modeling light extinction in samples heated above the solidus temperature not only because the optical properties of (Mg,Fe)O melt are unknown but also because of light scattering at melt-solid interfaces. Light scattering may become dominant in a nonhomogeneous sample, and its total light extinction coefficient is larger than the weighted sum of the absorption coefficients of the individual phases. The major challenge is to constrain the wavelength-dependence and angular direction of light scattering in a micron-thin sample with geometry that continuously changes above the solidus temperature. Therefore, our results do not have direct implications to temperature measurements in samples with melt fractions that significantly affect the system's optical properties.

Our results lend support to the hotter Fp solidus reported by Fu et al. (2018) whose melting curves (for Fp with 14 mol.% Fe) only cross the Earth's geotherm in the lowermost mantle and if the core-mantle boundary temperature (T_{CMB}) exceeds 4200 K. Current estimates of T_{CMB} are generally below 4200 K (Andrault et al., 2011; Fiquet et al., 2010; Nomura et al., 2014) but, in principle, T_{CMB} in excess of 4200 K are not ruled out (Anzellini et al., 2013). Therefore, our results suggest that Fp is unlikely to be globally molten near the CMB.

4. Conclusions

In this work we modeled the effect of the pressure-, temperature-, and wavelength-dependent optical properties of ferropericlase on temperature determination in laser-heated DAC experiments. Our results show that the community-wide graybody approximation contributes moderate (± 200 K) systematic error to the temperature determination in experiments where the maximum temperature does not exceed 2300 K. However, at the pressure-temperature conditions of the core-mantle boundary the graybody assumption may underestimate the temperature by up to 600 K in self-insulated samples. Our results suggest that the discrepancies in the reported solidus curves of ferropericlase are due to its strongly wavelength-dependent optical properties as well as the presence/absence of thermal insulation in the melting experiments. More generally, our study advocates for a new community-wide approach to temperature measurements in LH DACs beyond the graybody approximation. Toward this end, we will continue to measure the optical properties of relevant geological samples at mantle pressure-temperature conditions.

Acknowledgments
S. S. L. acknowledges the support of the Helmholtz Young Investigators Group CLEAR (VH-NG-1325). We thank Brent Grocholski for providing us with the ferropericlase sample. Alexander F. Goncharov and Monika Koch-Müller are thanked for their assistance in the spectroscopic measurements while Georg Spiekermann and Kanani K. M. Lee for their comments on their earlier versions of this manuscript. The authors declare no conflict of interest. Spectroscopic data associated with this paper are deposited at Mendeley Data (DOI: 10.17632/8jbfs7y8kh.1) and are also available as supporting information.

References

Akahama, Y., & Kawamura, H. (2006). Pressure calibration of diamond anvil Raman gauge to 310 GPa. *Journal of Applied Physics*, *100*(4), 043516.

Andersson, P. (1985). Thermal conductivity under pressure and through phase transitions in solid alkali halides. I. Experimental results for KCl, KBr, KI, RbCl, RbBr and RbI. *Journal of Physics C: Solid State Physics*, *18*(20), 3943–3955.

Andrault, D., Bolfan-Casanova, N., Lo Nigro, G., Bouhifd, M. A., Garbarino, G., & Mezouar, M. (2011). Solidus and liquidus profiles of chondritic mantle: Implication for melting of the Earth across its history. *Earth and Planetary Science Letters*, *304*(1-2), 251–259.

Andrault, D., Pesce, G., Bouhifd, M. A., Bolfan-Casanova, N., Henot, J. M., & Mezouar, M. (2014). Melting of subducted basalt at the core-mantle boundary. *Science*, *344*(6186), 892–895. https://doi.org/10.1126/science.1250466

Anzellini, S., Dewaele, A., Mezouar, M., Loubeyre, P., & Morard, G. (2013). Melting of iron at Earth's inner core boundary based on fast X-ray diffraction. *Science*, *340*(6131), 464–466. https://doi.org/10.1126/science.1233514

Badro, J. (2014). Spin transitions in mantle minerals. *Annual Review of Earth and Planetary Sciences*, *42*, 231–248.

Badro, J., Fiquet, G., Guyot, F., Rueff, J. P., Struzhkin, V. V., Vanko, G., & Monaco, G. (2003). Iron partitioning in Earth's mantle: Toward a deep lower mantle discontinuity. *Science*, *300*(5620), 789–791. https://doi.org/10.1126/science.1081311

Benedetti, L. R., Guignot, N., & Farber, D. L. (2007). Achieving accuracy in spectroradiometric measurements of temperature in the laser-heated diamond anvil cell: Diamond is an optical component. *Journal of Applied Physics*, *101*(1), 013109.

Benedetti, L. R., & Loubeyre, P. (2004). Temperature gradients, wavelength-dependent emissivity, and accuracy of high and very-high temperatures measured in the laser-heated diamond cell. *High Pressure Research*, *24*(4), 423–445.

Bodea, S., & Jeanloz, R. (1989). Model calculations of the temperature distribution in the laser-heated diamond cell. *Journal of Applied Physics*, *65*(12), 4688–4692.

Bower, D. J., Wicks, J. K., Gurnis, M., & Jackson, J. M. (2011). A geodynamic and mineral physics model of a solid-state ultralow-velocity zone. *Earth and Planetary Science Letters*, *303*(3-4), 193–202.
Burns, R. G. (1993). *Mineralogical applications of crystal field theory* (2nd ed.). UK.: Cambridge University Press.
Campbell, A. J. (2008). Measurement of temperature distributions across laser heated samples by multispectral imaging radiometry. *Review of Scientific Instruments*, *79*(1), 015108. https://doi.org/10.1063/1.2827513
Deng, J., Du, Z. X., Benedetti, L. R., & Lee, K. K. M. (2017). The influence of wavelength-dependent absorption and temperature gradients on temperature determination in laser-heated diamond-anvil cells. *Journal of Applied Physics*, *121*(2), 025901.
Deng, J., & Lee, K. K. M. (2017). Viscosity jump in the lower mantle inferred from melting curves of ferropericlase. *Nature Communications*, *8*, 1997.
Deng, J., & Lee, K. K. M. (2019). Melting temperature depression due to electronic spin transition of iron. *American Mineralogist*, *104*, 1189–1196.
Dewaele, A., Belonoshko, A. B., Garbarino, G., Occelli, F., Bouvier, P., Hanfland, M., & Mezouar, M. (2012). High-pressure high-temperature equation of state of KCl and KBr. *Physical Review B*, *85*(21), 214105.
Dziewonski, A. M., & Anderson, D. L. (1981). Preliminary Reference Earth Model. *Physics of the Earth and Planetary Interiors*, *25*(4), 297–356.
Fiquet, G., Auzende, A. L., Siebert, J., Corgne, A., Bureau, H., Ozawa, H., & Garbarino, G. (2010). Melting of peridotite to 140 gigapascals. *Science*, *329*(5998), 1516–1518.
Fu, S. Y., Yang, J., Zhang, Y. J., Liu, J. C., Greenberg, E., Prakapenka, V. B., et al. (2018). Melting behavior of the lower-mantle ferropericlase across the spin crossover: Implication for the ultra-low velocity zones at the lowermost mantle. *Earth and Planetary Science Letters*, *503*, 1–9. https://doi.org/10.1016/j.epsl.2018.09.014
Giampaoli, R., Kantor, I., Mezouar, M., Boccato, S., Rosa, A. D., Torchio, R., et al. (2018). Measurement of temperature in the laser heated diamond anvil cell: comparison between reflective and refractive optics. *High Pressure Research*, *38*(3), 250–269. https://doi.org/10.1080/08957959.2018.1480017
Glazyrin, K., Miyajima, N., Smith, J. S., & Lee, K. K. M. (2016). Compression of a multiphase mantle assemblage: Effects of undesirable stress and stress annealing on the iron spin state crossover in ferropericlase. *Journal of Geophysical Research: Solid Earth*, *121*, 3377–3392.
Gomez-Perez, N., Rodriguez, J. F., & McWilliams, R. S. (2017). Finite element modeling of melting and fluid flow in the laser-heated diamond-anvil cell. *Journal of Applied Physics*, *121*(14), 145904.
Goncharov, A. F., Beck, P., Struzhkin, V. V., Haugen, B. D., & Jacobsen, S. D. (2009). Thermal conductivity of lower-mantle minerals. *Physics of the Earth and Planetary Interiors*, *174*(1-4), 24–32.
Goncharov, A. F., Lobanov, S. S., Tan, X., Hohensee, G. T., Cahill, D. G., Lin, J. F., et al. (2015). Experimental study of thermal conductivity at high pressures: Implications for the deep Earth's interior. *Physics of the Earth and Planetary Interiors*, *247*, 11–16. https://doi.org/10.1016/j.pepi.2015.02.004
Goncharov, A. F., Struzhkin, V. V., & Jacobsen, S. D. (2006). Reduced radiative conductivity of low-spin (Mg,Fe)O in the lower mantle. *Science*, *312*(5777), 1205–1208. https://doi.org/10.1126/science.1125622
Grocholski, B., Catalli, K., Shim, S. H., & Prakapenka, V. (2012). Mineralogical effects on the detectability of the postperovskite boundary. *Proceedings of the National Academy of Sciences of the United States of America*, *109*(7), 2275–2279. https://doi.org/10.1073/pnas.1109204109
Hasegawa, A., Yagi, T., & Ohta, K. (2019). Combination of pulsed light heating thermoreflectance and laser-heated diamond anvil cell for in-situ high pressure-temperature thermal diffusivity measurements. *Review of Scientific Instruments*, *90*(7), 074901.
Holmstrom, E., & Stixrude, L. (2015). Spin crossover in ferropericlase from first-principles molecular dynamics. *Physical Review Letters*, *114*(11), 117202. https://doi.org/10.1103/PhysRevLett.114.117202
Johannsen, P. G., Reiss, G., Bohle, U., Magiera, J., Muller, R., Spiekermann, H., & Holzapfel, W. B. (1997). Refractive index of the alkali halides.2. Effect of pressure on the refractive index of 11 alkali halides. *Physical Review B*, *55*(11), 6865–6870.
Kavner, A., & Panero, W. R. (2004). Temperature gradients and evaluation of thermoelastic properties in the synchrotron-based laser-heated diamond cell. *Physics of the Earth and Planetary Interiors*, *143*, 527–539.
Keppler, H., Dubrovinsky, L. S., Narygina, O., & Kantor, I. (2008). Optical absorption and radiative thermal conductivity of silicate perovskite to 125 gigapascals. *Science*, *322*(5907), 1529–1532. https://doi.org/10.1126/science.1164609
Keppler, H., Kantor, I., & Dubrovinsky, L. S. (2007). Optical absorption spectra of ferropericlase to 84 GPa. *American Mineralogist*, *92*(2-3), 433–436.
Keppler, H., Mccammon, C. A., & Rubie, D. C. (1994). Crystal-field and charge-transfer spectra of (Mg,Fe)SiO_3 perovskite. *American Mineralogist*, *79*(11-12), 1215–1218.
Keppler, H., & Smyth, J. R. (2005). Optical and near infrared spectra of ringwoodite to 21.5 GPa: Implications for radiative heat transport in the mantle. *American Mineralogist*, *90*(7), 1209–1212.
Kiefer, B., & Duffy, T. S. (2005). Finite element simulations of the laser-heated diamond-anvil cell. *Journal of Applied Physics*, *97*(11), 114902.
Konopkova, Z., McWilliams, R. S., Gomez-Perez, N., & Goncharov, A. F. (2016). Direct measurement of thermal conductivity in solid iron at planetary core conditions. *Nature*, *534*(7605), 99–101. https://doi.org/10.1038/nature18009
Kunz, M., Yan, J. Y., Cornell, E., Domning, E. E., Yen, C. E., Doran, A., et al. (2018). Implementation and application of the peak scaling method for temperature measurement in the laser heated diamond anvil cell. *Review of Scientific Instruments*, *89*(8), 083903. https://doi.org/10.1063/1.5028276
Li, B., Ji, C., Yang, W. G., Wang, J. Y., Yang, K., Xu, R. Q., et al. (2018). Diamond anvil cell behavior up to 4 Mbar. *Proceedings of the National Academy of Sciences of the United States of America*, *115*(8), 1713–1717. https://doi.org/10.1073/pnas.1721425115
Lin, J. F., Gavriliuk, A. G., Struzhkin, V. V., Jacobsen, S. D., Sturhahn, W., Hu, M. Y., et al. (2006). Pressure-induced electronic spin transition of iron in magnesiowustite-(Mg,Fe)O. *Physical Review B*, *73*(11), 113107.
Lin, J. F., Speziale, S., Mao, Z., & Marquardt, H. (2013). Effects of the electronic spin transitions of iron in lower mantle minerals: Implications for deep mantle geophysics and geochemistry. *Reviews of Geophysics*, *51*, 244–275.
Lin, J. F., Vanko, G., Jacobsen, S. D., Iota, V., Struzhkin, V. V., Prakapenka, V. B., et al. (2007). Spin transition zone in Earth's lower mantle. *Science*, *317*(5845), 1740–1743. https://doi.org/10.1126/science.1144997
Lobanov, S. S., Goncharov, A. F., & Litasov, K. D. (2015). Optical properties of siderite ($FeCO_3$) across the spin transition: Crossover to iron-rich carbonates in the lower mantle. *American Mineralogist*, *100*(5-6), 1059–1064.
Lobanov, S. S., Holtgrewe, N., & Goncharov, A. F. (2016). Reduced radiative conductivity of low spin FeO_6-octahedra in $FeCO_3$ at high pressure and temperature. *Earth and Planetary Science Letters*, *449*, 20–25.

Lobanov, S. S., Holtgrewe, N., Lin, J. F., & Goncharov, A. F. (2017). Radiative conductivity and abundance of post-perovskite in the lowermost mantle. *Earth and Planetary Science Letters*, *479*, 43–49.
Lobanov, S. S., Hsu, H., Lin, J. F., Yoshino, T., & Goncharov, A. F. (2017). Optical signatures of low spin Fe^{3+} in NAL at high pressure. *Journal of Geophysical Research: Solid Earth*, *122*, 3565–3573.
Lobanov, S. S., Soubiran, F., Holtgrewe, N., Badro, J., Lin, J. F., & Goncharov, A. F. (2019). Opaque Lowermost Mantle. *arXiv:1909.01438*, https://arxiv.org/abs/1909.01438.
Manga, M., & Jeanloz, R. (1996). Axial temperature gradients in dielectric samples in the laser-heated diamond cell. *Geophysical Research Letters*, *23*(14), 1845–1848.
McMahon, H. O. (1950). Thermal Radiation from Partially Transparent Reflecting Bodies. *Journal of the Optical Society of America*, *40*(6), 376–380.
McWilliams, R. S., Konopkova, Z., & Goncharov, A. F. (2015). A flash heating method for measuring thermal conductivity at high pressure and temperature: Application to Pt. *Physics of the Earth and Planetary Interiors*, *247*, 17–26.
Megnin, C., & Romanowicz, B. (2000). The three-dimensional shear velocity structure of the mantle from the inversion of body, surface and higher-mode waveforms. *Geophysical Journal International*, *143*(3), 709–728.
Ming, L. C., & Bassett, W. A. (1974). Laser heating in the diamond anvil press up to 2000°C sustained and 3000°C pulsed at pressures up to 260 kilobars. *Review of Scientific Instruments*, *45*(9), 1115–1118.
Montoya, J. A., & Goncharov, A. F. (2012). Finite element calculations of the time dependent thermal fluxes in the laser-heated diamond anvil cell. *Journal of Applied Physics*, *111*(11), 112617.
Nomura, R., Hirose, K., Uesugi, K., Ohishi, Y., Tsuchiyama, A., Miyake, A., & Ueno, Y. (2014). Low core-mantle boundary temperature inferred from the solidus of pyrolite. *Science*, *343*(6170), 522–525. https://doi.org/10.1126/science.1248186
Ohta, K., Hirose, K., Ichiki, M., Shimizu, K., Sata, N., & Ohishi, Y. (2010). Electrical conductivities of pyrolitic mantle and MORB materials up to the lowermost mantle conditions. *Earth and Planetary Science Letters*, *289*(3-4), 497–502.
Ohta, K., Yagi, T., Hirose, K., & Ohishi, Y. (2017). Thermal conductivity of ferropericlase in the Earth's lower mantle. *Earth and Planetary Science Letters*, *465*, 29–37.
Ohta, K., Yagi, T., Taketoshi, N., Hirose, K., Kornabayashi, T., Baba, T., et al. (2012). Lattice thermal conductivity of $MgSiO_3$ perovskite and post-perovskite at the core-mantle boundary. *Earth and Planetary Science Letters*, *349*, 109–115.
Okuda, Y., Ohta, K., Yagi, T., Sinmyo, R., Wakamatsu, T., Hirose, K., & Ohishi, Y. (2017). The effect of iron and aluminum incorporation on lattice thermal conductivity of bridgmanite at the Earth's lower mantle. *Earth and Planetary Science Letters*, *474*, 25–31.
Panero, W. R., & Jeanloz, R. (2001). Temperature gradients in the laser-heated diamond anvil cell. *Journal of Geophysical Research*, *106*(B4), 6493–6498.
Petitgirard, S., Salamat, A., Beck, P., Weck, G., & Bouvier, P. (2014). Strategies for in situ laser heating in the diamond anvil cell at an X-ray diffraction beamline. *Journal of Synchrotron Radiation*, *21*(Pt 1), 89–96. https://doi.org/10.1107/S1600577513027434
Piet, H., Badro, J., Nabiei, F., Dennenwaldt, T., Shim, S. H., Cantoni, M., et al. (2016). Spin and valence dependence of iron partitioning in Earth's deep mantle. *Proceedings of the National Academy of Sciences of the United States of America*, *113*(40), 11,127–11,130. https://doi.org/10.1073/pnas.1605290113
Prakapenka, V. B., Kubo, A., Kuznetsov, A., Laskin, A., Shkurikhin, O., Dera, P., et al. (2008). Advanced flat top laser heating system for high pressure research at GSECARS: application to the melting behavior of germanium. *High Pressure Research*, *28*(3), 225–235. https://doi.org/10.1080/08957950802050718
Rainey, E. S. G., Hernlund, J. W., & Kavner, A. (2013). Temperature distributions in the laser-heated diamond anvil cell from 3-D numerical modeling. *Journal of Applied Physics*, *114*(20), 204905.
Shankland, T. J., Nitsan, U., & Duba, A. G. (1979). Optical absorption and radiative heat transport in olivine at high temperature. *Journal of Geophysical Research*, *84*, 1603–1610.
Shim, S. H., Duffy, T. S., & Shen, G. Y. (2001). The post-spinel transformation in Mg_2SiO_4 and its relation to the 660-km seismic discontinuity. *Nature*, *411*(6837), 571–574. https://doi.org/10.1038/35079053
Speziale, S., Milner, A., Lee, V. E., Clark, S. M., Pasternak, M. P., & Jeanloz, R. (2005). Iron spin transition in Earth's mantle. *Proceedings of the National Academy of Sciences of the United States of America*, *102*(50), 17,918–17,922.
Sturhahn, W., Jackson, J. M., & Lin, J. F. (2005). The spin state of iron in minerals of Earth's lower mantle. *Geophysical Research Letters*, *32*, L12307. https://doi.org/10.1029/2005GL022802
Syassen, K. (2008). Ruby under pressure. *High Pressure Research*, *28*(2), 75–126.
Tange, Y., Nishihara, Y., & Tsuchiya, T. (2009). Unified analyses for P-V-T equation of state of MgO: A solution for pressure-scale problems in high P-T experiments. *Journal of Geophysical Research*, *114*, B03208. https://doi.org/10.1029/2008JB005813
Thomas, S. M., Bina, C. R., Jacobsen, S. D., & Goncharov, A. F. (2012). Radiative heat transfer in a hydrous mantle transition zone. *Earth and Planetary Science Letters*, *357*, 130–136.
Tsuchiya, T., Wentzcovitch, R. M., da Silva, C. R. S., & de Gironcoli, S. (2006). Spin transition in magnesiowustite in Earth's lower mantle. *Physical Review Letters*, *96*(19), 198501. https://doi.org/10.1103/PhysRevLett.96.198501
Ullrich, K., Langer, K., & Becker, K. D. (2002). Temperature dependence of the polarized electronic absorption spectra of olivines. Part I—Fayalite. *Physics and Chemistry of Minerals*, *29*(6), 409–419.
Walter, M. J., & Koga, K. T. (2004). The effects of chromatic dispersion on temperature measurement in the laser-heated diamond anvil cell. *Physics of the Earth and Planetary Interiors*, *143*, 541–558.
Wicks, J. K., Jackson, J. M., Sturhahn, W., & Zhang, D. Z. (2017). Sound velocity and density of magnesiowustites: Implications for ultralow-velocity zone topography. *Geophysical Research Letters*, *44*, 2148–2158.
Williams, Q., & Garnero, E. J. (1996). Seismic evidence for partial melt at the base of Earth's mantle. *Science*, *273*(5281), 1528–1530.
Yuan, K. Q., & Romanowicz, B. (2017). Seismic evidence for partial melting at the root of major hot spot plumes. *Science*, *357*(6349), 393–397. https://doi.org/10.1126/science.aan0760
Zerr, A., Diegeler, A., & Boehler, R. (1998). Solidus of Earth's deep mantle. *Science*, *281*(5374), 243–246.

Erratum

The originally published version of equation (1) contained typographical errors. These errors did not affect the results or conclusions of the paper, because the correct version of equation (1) was used in the work. The errors have been corrected, and this may be considered the official version of record.